Desalination and Water Treatment
www.deswater.com
doi: 10.5004/dwt.2023.30117

314 (2023) 185–198
December

Removal of cesium by batch and fixed bed column methods using a new nano-composite based on O-carboxymethyl chitosan and nano copper potassium hexacyanoferrate

Dalia A. Fadel[a,*], Mohamed M. Azab[b], Amal M. Metwally[b], Fathia A. Abdelghany[b], Hanaa A. ElKhawaga[c]

[a]*Reactors Department, Nuclear Research Center, Egyptian Atomic Energy Authority, P.O.: 13759, Inshas, Cairo, Egypt, email: dalia_shaaban@windowslive.com*
[b]*Chemistry Department, Faculty of Science, Benha University, Benha, Egypt, emails: mohamed.azab01@fsc.bu.edu.eg (M.M. Azab), aml.metwaly@fsc.bu.edu.eg (A.M. Metwally), fathiaahmed193@gmail.com (F.A. Abdelghany)*
[c]*Faculty of Engineering (Shoubra), Benha University, Benha, Egypt, email: hana.abdelazim@feng.bu.edu.eg*

Received 26 July 2023; Accepted 28 October 2023

ABSTRACT

A novel type of ion exchanger polymer nanocomposite was achieved and applied for the removal of Cs^+ ions from aqueous media. The ion exchanger polymer nanocomposite was prepared based on natural polymer with some chemical modification. The reaction was followed by three steps to prepare the ion exchanger, the first step including the preparation of O-carboxymethyl chitosan (O-CMC), while the second step is the formation of copper potassium hexacyanoferrates nanoparticles (CuKHCF). Finally, the prepared CuKHCF was introducing through polymer matrix of O-CMC to obtain CuKHCF/O-CMC. By Fourier-transform infrared spectroscopy, the composition of the prepared compounds was elucidated. The surface morphology of nanoparticles of CuKHCF and ion exchanger was reported by scanning electron microscopy. Also, transmission electron microscopy was used to report the morphology. Also, the thermal stability was studied using thermogravimetric analysis. A sorption behavior of the ion exchanger toward removal of Cs^+ ions from aqueous media was studied at different solution pH, different initial concentration of Cs^+ ions, time that Cs^+ ions contact with ion exchanger and temperature of solution through batch experiments. From obtained results, the highest capacity was 1.71 mmol/g for Cs^+ ions at initial concentration 10 mmol/L and shaking time 2 h at temperature 25°C. By studying the adsorption isotherms and the kinetics, Langmuir model and pseudo-second-order were fitted with this process. Through the data obtained thermodynamic parameters, the nature of sorption process is spontaneous and also endothermic. Also, the sorption process was also achieved by column technique. At pH 7 and an initial concentration of 4 mmoL, the impact of bed depth and flow rate on the adsorption properties of the composite was investigated. Models of Thomas and Yoon–Nelson were employed to assess the performance of the column adsorption. Additionally, it has been shown that 2.0 M KCl may successfully desorb loaded Cs^+. Lastly, the synthetic composite was applied successfully five times.

Keywords: O-carboxymethyl chitosan; Cesium; Adsorption; Batch; Langmuir; Pseudo-second-order; Column technique; Bed depth

* Corresponding author.

1. Introduction

The nuclear sector is expanding quickly in response to the world's rising energy needs, but this also raises the issue of how to adequately deal with radioactive waste. Through the fission of ^{235}U in nuclear waste, ^{137}Cs is created as radioactive elements. ^{137}Cs radioactive is characterized through long a half-life of around 30.17 y and with a highly thermal fission nuclide [1,2]. High biological toxicity, great migratory ability, and solubility are all characteristics of $^{137}Cs^+$. Some organisms were damaged such as liver, central nervous system and kidneys through the bioaccumulation of $^{137}Cs^+$ in soft tissues after it penetrates the human body [3]. Additionally, ^{137}Cs is extensively utilized in the domains of agriculture, industry, and medicine [4–6]. In order to get rid of these problems causing for human health and environment, it is crucial to efficiently extract and recover radio cesium from radioactive wastewater. Due to it is easily to transfer and effect of other interfering ions, the effective extraction of $^{137}Cs^+$ from complex solutions continues to be a significant issue.

Cs^+ ions can be removed from aqueous solutions different techniques such as coprecipitation [7], solvent extraction [8], reverse osmosis [9], adsorption process [10] and ion exchange [11].

One of the materials which are characterized by high selectivity and good efficient for Cs^+ sorption in aqueous media is the transition metal hexacyanoferrates (MHCFs) [12]. Due to the similarity between lattice spacing of MHCFs with hydrated Cs^+ ion size (3.25 Å), this increase the ability of MHCFs for removing Cs^+ ion [13,14]. A fine powder shape MHCFs caused problem observed in using for the removal Cs^+, which is the difficulty of removing these particles from water by filtration or centrifugation; so, introducing these particles in supporting polymeric materials is necessary. MHCFs can be introduced through carboxymethyl cellulose [15,16], polyvinyl alcohol [17–20], alginate [21] or chitosan [22,23] as supporting materials. The introducing of MHCF nanoparticles in polymer matrix was supported by presence of functional groups. Such polymer is chitosan, which have some advantages such as cost-effectiveness, availability, and multifunctional groups for desalination by ion adsorption [24–26]. The low mechanical properties and low acidic stability of pure chitosan decrease the ability for using in a real adsorption process [27–30]. To overcome this defect, the crosslinking process of chitosan is necessary [31]. This crosslinking decrease the active sites and the adsorption nature of the chitosan, which decrease the number amino groups.

In this research, a novel type of ion exchanger nanocomposite based on introducing of copper potassium hexacyanoferrate (CuKHCF) nanoparticles in O-carboxymethyl chitosan (O-CMC) as polymer matrix was achieved and applied for removal of Cs from aqueous media. The ion exchanger polymer nanocomposite was obtained based on natural polymer with some chemical modification. By Fourier-transform infrared spectroscopy (FTIR), the composition of the prepared compounds was elucidated, whereas the surface morphology of nanoparticles of CuKHCF and ion exchanger was reported by scanning electron microscopy (SEM) and transmission electron microscopy (TEM). Also, the thermal behavior was studied by thermogravimetric analysis (TGA). The adsorption behavior of the prepared ion exchanger toward Cs^+ ions in aqueous media was studied through batch experiments and column techniques.

2. Synthesis and characterization techniques

2.1. Chemicals

From Merck (India), chitosan was obtained with degree of acetylation was 0.25. Monochloroacetic acid and isopropanol were supplied from Sigma-Aldrich (United States). Chloride of nickel ($NiCl_2{\cdot}6H_2O$), sulfate of copper ($CuSO_4{\cdot}5H_2O$), potassium hexacyanoferrate ($K_4Fe(CN)_6{\cdot}3H_2O$) and NaOH were obtained from Alfa Aesar (China). Cesium chloride (CsCl), which is non-radioactive and was acquired from Alfa Aesar (China), was substituted for ^{137}Cs due to its chemical similarities. Without additional purification, all compounds were used.

2.2. Synthesis

2.2.1. Synthesis of the nanoparticles of copper hexacyanoferrate

Nanoparticles from CuKHCF was prepared as follows: a solution of $CuSO_4{\cdot}5H_2O$ (10 wt.%) was added dropwise with stirring into a solution of $K_4Fe(CN)_6{\cdot}3H_2O$ (10 wt.%). Dropwise the solution of polyvinyl alcohol (PVA) (6% in 100 mL of distilled water) to the above solution and then left for stirring for 24 h in room temperature. Fine powder of CuKHCF nanoparticles was filtered and distilled water was used in washing and then CuKHCF nanoparticles were dried in room temperature.

2.2.2. Synthesis of O-carboxymethyl chitosan

O-CMC was synthesized by mixing 10 g chitosan (Cs) in a solution of NaOH (13.5 g in 25 mL distilled water) and 100 mL isopropanol and then left for stirring for 1 h at 30°C. After 1 h, chloroacetic acid solution (15 g in 20 mL of isopropanol) was added dropwise to mixture and the reaction was stopped by addition of 200 mL of 95% ethyl alcohol. O-CMC was filtrated and dried at temperature 50°C.

2.2.3. Synthesis of CuKHCF/O-CMC nanocomposite

CuKHCF/O-CMC nanocomposite was obtained through the dissolving of 2 g of O-CMC in 100 mL distilled water and then mixed with a solution of 3 g CuKHCF in 100 mL distilled water with continuous stirring for 24 h. Then solution of $NiCl_2$ was added with stirring for 3 h. Stand the reaction to 3 days. Finally, the nanocomposite was taken out, with washing by water and at room temperature it dried.

2.3. Adsorption of cesium ions by batch method

For the studies, the tests were carried out with 0.1 g of CuKHCF/O-CMC nanocomposite in 100 mL of cesium solution and shake in shaker controlled at 250 rpm at room temperature except studies at various temperatures. After equilibrium, CuKHCF/O-CMC was removed from cesium

solutions after adsorption experiments using a centrifuge. Hitachi Atomic Absorption Z-6100 Polarized Zeeman (United Kingdom) is used for detecting the remaining cesium ion concentrations in solutions were determined by. The pH of solutions was controlled through using a few drops of HCl or NaOH. By using Eq. (1) [32], the capacity (q_e) (mmol/g) for the sorption process at equilibrium can be calculated.

$$q = \frac{\left(C_0 - C_e\right)V}{W} \tag{1}$$

where C_0 and C_e (mmol/L) are the concentrations of Cs^+ at initial and equilibrium, respectively. V (L) is volume taken from Cs solution in experiment. The weight of ion exchanger is expressed through W (g).

2.4. Cesium adsorption using fixed-bed column technique

As a way to create a uniform and tightly packed bed, CuKHCF/O-CMC was added to a glass column of 12 mm and length of 20 cm and used in a continuous adsorption experiment. A breakthrough curve was employed to explain the performance of fixed bed column and was used to represent standard concentration, which represents the ratio of effluent metal concentration to influent metal concentration (C_{eff}/C_o) vs. time (t), which C_{eff} and C_o represent the cesium ions from the effluent and influent concentrations (mmol/L), respectively. Adsorption tests at various bed heights (0.8, 1.6, and 2.4 cm), 4 mmol/L individual metal ion concentration, pH 7, and ambient temperature were performed in order to optimize the column dynamic. At a constant bed depth of 1.6 cm, the effect of flow rate (1.0 and 3 mL/min) was investigated. To eliminate air bubbles and clean the adsorbent, sufficient deionized water was used to wash the column initially in an up-flow mode. A peristaltic pump (Pump Drive 5101, Heidolph, Schwabach, Germany) was used to measure the flow rate. The atomic absorption spectroscopy was employed to calculate the concentration of residual metal ions in the effluent. The region beneath the graph of adsorbed ions concentration (C_{ads}) (mmol/L) vs. time (min) was employed to illustrate the total quantity of metal ions adsorbed (q_{total}, mmoL) [33,34]. Given by Eq. (2) was the mass transfer zone (Δt) [34].

$$\Delta t = t_e - t_b \tag{2}$$

where t_b represents the breakthrough time and t_e represents the bed exhaustion time.

Eq. (3) was used to determine the mass transfer zone's length, Z_m [34].

$$Z_m = Z\left(1 - \frac{t_b}{t_e}\right) \tag{3}$$

where Z denotes the height of the bed in centimeters. From Eq. (4), the total column adsorption capacity (q_{total}) [34] was determined.

$$q_{total} = \frac{FA}{1000} = \frac{F}{1000}\int_{t=0}^{t=t_{total}} \left(C_{ads}\right)dt \tag{4}$$

where A represents the region beneath the plot's breakthrough curve between C_{ad} ($C_{ad} = C_0 - C_{eff}$) vs. time (t), t_{total} (min) represents the total flow time, and F (mL/min) is the volumetric rate of flow in mL/min, which might be derived using a division of the effluent volume (V_{eff}, mL) by the total duration (t_{total}, min). Eq. (5) determines the volumetric flow rate F [34].

$$F = \frac{V_{eff}}{t_{total}} \tag{5}$$

Eq. (6) was used to get the capacity for equilibrium adsorption ($q_{e(exp)}$) (mmol/g) [34].

$$q_{e(exp)} = \frac{q_{total}}{W} \tag{6}$$

where W is the O-CMC-CuKFe(CN)$_6$ total dry weight, g. Eq. (7) was employed to determine the total quantity of metal ions provided to the column, m_{total} (mmoL) [34].

$$m_{total} = \frac{C0Ft_{total}}{1000} \tag{7}$$

According to Eq. (8) [34], the total percentage removal R (%) of Cs^+ has been given.

$$R(\%) = \frac{q_{total}}{m_{total}} \times 100 \tag{8}$$

2.5. Regeneration of columns

During the elution method, 300 mL of a 2.0 M KCl solution were employed as the eluent and were passed down a glass column at 5 mL/min flow rate. Following every single adsorption–desorption cycle, the O-CMC-CuKFe(CN)$_6$ composite was painstakingly cleaned using deionized water once again in order to regenerate subsequent studies. Again, the column supplied using an influent solution under the following experimental circumstances: starting pH is 7, flow is 1 mL/min, and the bed height is 1.6 cm with a concentration of 4 mmol/L. Adsorption–desorption experiments including 5 cycles were performed to evaluate the O-CMC-CuKFe(CN)$_6$ composite's reusability.

2.6. Characterization techniques

In the KBr phase, FTIR for CuKHCF nanoparticles, O-CMCs and CuKHCF/O-CMCs were identified (Shimadzu 8201 PC). The TGA studies for CuKHCF/O-CMCs were investigated in a dynamic atmosphere of nitrogen through SDT Q600 V20.9 Build 20, USA. The CuKHCF and CuKHCF/O-CMCs morphology was reported using a Quanta FEG scanning electron microscope-energy-dispersive X-ray spectroscopy (SEM-EDX), USA. Also, CuKHCF morphology and particle size were estimated through TEM (JEOL JEM-1230 TEM, USA). X-ray diffraction (XRD) of CuKHCF nanoparticles and CuKHCF/O-CMCs composite were investigated with a Diano X-ray Diffractometer (Germany).

3. Results and discussion

3.1. Synthesis of CuKHCF/O-CMC nanocomposite

Fig. 1 shows that the ion exchanger polymer nanocomposite (CuKHCF/O-CMC) was prepared based on natural polymer with some chemical modification. The reaction followed by three steps to prepare the ion exchanger, the first step including the formation of O-CMC, the second step is the formation copper potassium hexacyanoferrates nanoparticles (CuKHCF) and finally the prepared CuKHCF was incorporated through polymer matrix of O-CMC to obtain CuKHCF/O-CMC. Fig. 2 showed the ion exchange process between potassium and cesium ions.

3.2. Characterization

3.2.1. FTIR spectra of the prepared materials

The spectra of FTIR of O-CMC, CuKHCF nanoparticles and CuKHCF/O-CMC nanocomposite are shown in Fig. 3a–c. For O-CMC Fig. 3a shows absorption band at 1,630 cm^{-1} for carbonyl group (C=O) present in carboxyl methyl group, C–H bend appeared at 1,417 cm^{-1}, oxygen bridge stretch at 1,144 cm^{-1} and band at 1,064 cm^{-1} for C–O stretch. Fig. 3b shows CuKHCF nanoparticles spectrum, which strong peak at 2,079 cm^{-1} for the C≡N group and the Fe–C stretching appeared at region of 476–593 cm^{-1}. Fig. 3c exhibits the spectrum of CuKHCF/O-CMC nanocomposite, two strong peaks at 1,627 cm^{-1} for C=O group in carboxyl methyl group and 2,097 cm^{-1} for the C≡N similar to appear in O-CMC and in CuKHCF nanoparticles, respectively. From the presence of these bands proved the introducing of CuKHCF nanoparticles into O-CMC.

3.2.2. Morphological studies

The morphology for CuKHCF nanoparticles and also particle size were reported through studying by SEM and TEM. Fig. 4a and b show the nanoscale of the obtained CuKHCF (10–50 nm), which also the cubic shape was observed. Through SEM images, the morphology of CuKHCF/O-CMC nanocomposite was observed in two cases (before and after treatment with Cs solution) (Fig. 5a and c). Before treatment with cesium solution, there is uniformly distributed of CuKHCF nanoparticles through O-CMC (Fig. 5a). After treatment of nanocomposite with cesium solution, the surface becomes brighter due to the uniformly distributed of cesium ions after ion exchange with potassium ions (Fig. 5c). By EDX spectrum analysis, the mechanism of exchange between Cs ions and K^+ ions can be proved. Fig. 5b and d show the EDX spectra of CuKHCF/O-CMC nanocomposite before and after treatment with cesium solution, respectively. The percentage of K^+ ions in CuKHCF/O-CMC nanocomposite before treatment with cesium solution can be estimated through spectrum in Fig. 5b, whereas this percentage decreased in CuKHCF/O-CMC nanocomposite after adsorption of Cs^+ ions and new peak related to Cs ions appeared (Fig. 5d). The decrease in percentage in K^+ ions and appearing peak for Cs^+ ions proved ion exchange mechanism between K^+ ions found in nanocomposite and Cs^+ ions found in aqueous media.

3.2.3. X-ray diffraction

XRD for CuKHCF nanoparticles and CuKHCF/O-CMC nanocomposite are shown in Fig. 6a–c. Fig. 6a shows XRD for CuKHCF nanoparticles, which showed peaks at 2θ of 17.5°,

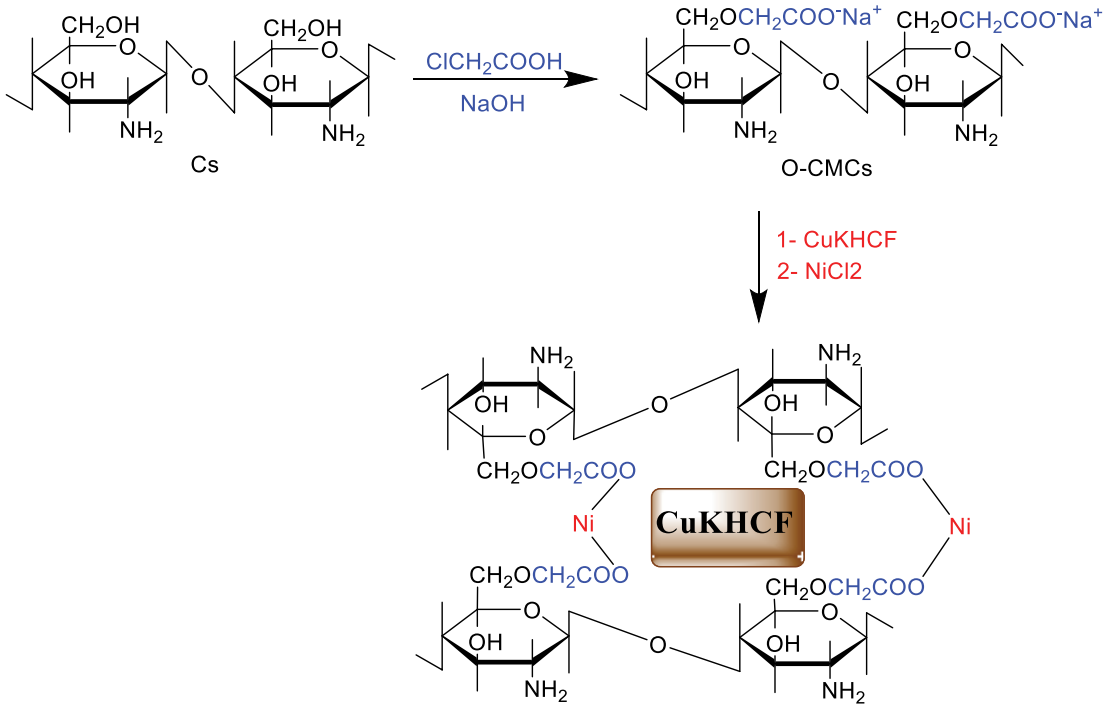

Fig. 1. Synthesis of ion exchanger polymer nanocomposite (CuKHCF/O-CMC).

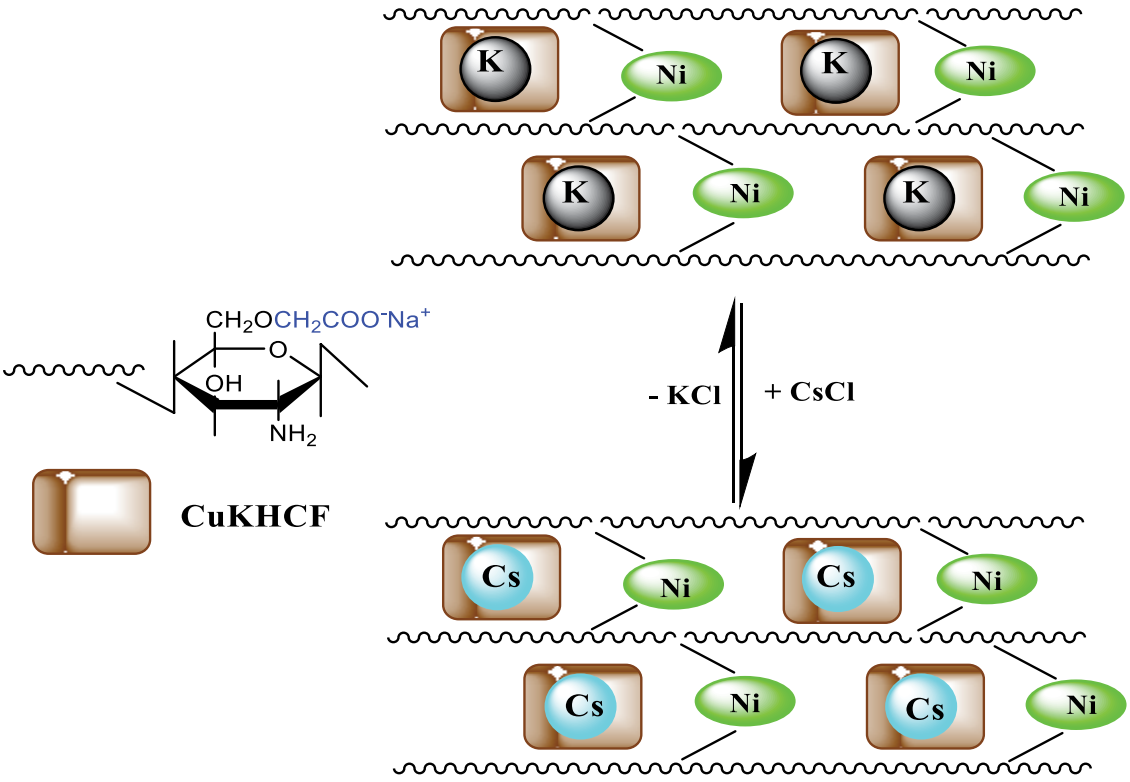

Fig. 2. Mechanism of ion exchange process between K^+ ions in nanocomposite and Cs^+ ions in aqueous media.

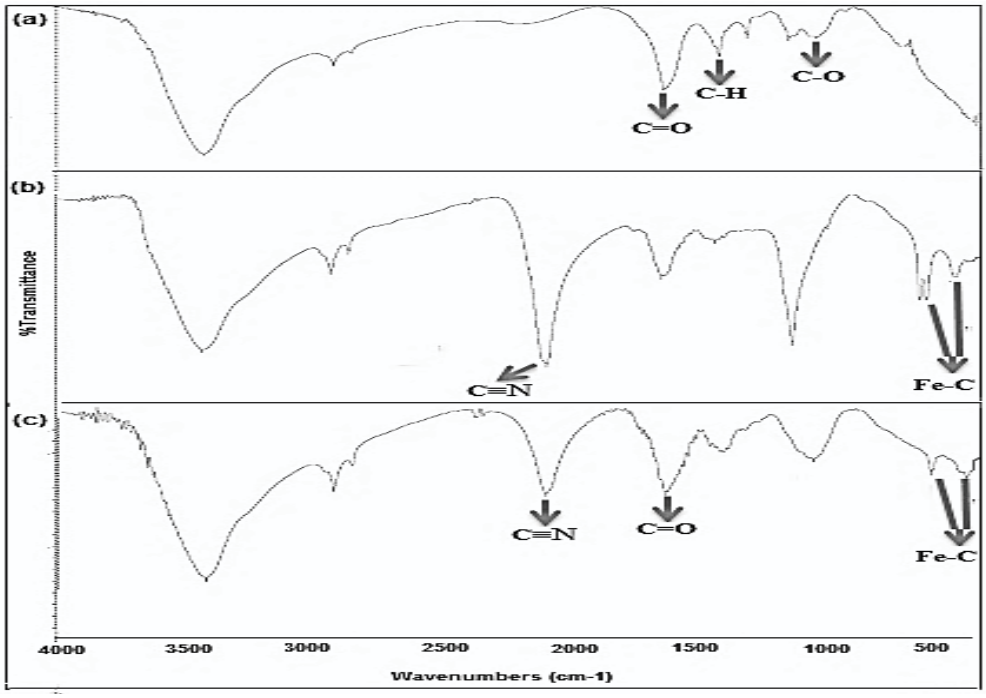

Fig. 3. Fourier-transform infrared spectroscopy for (a) O-CMC, (b) CuKHCF nanoparticles and (c) CuKHCF/O-CMC nanocomposite.

24.9°, 35.9°, 40.1°, 44.2°, and 51.1° according Miller indexes of (200), (220), (400), (420), (424), and (440), respectively [35] due to cubic crystal structure of CuKHCF. Fig. 6b shows XRD for O-CMC, which showed peaks at 2θ of 15.78, 20.15, 27.77, 33.01, 37.19, 45.50, 56.53 and 66.28. Fig. 6c shows the XRD patterns for prepared nanocomposite (CuKHCF/O-CMC),

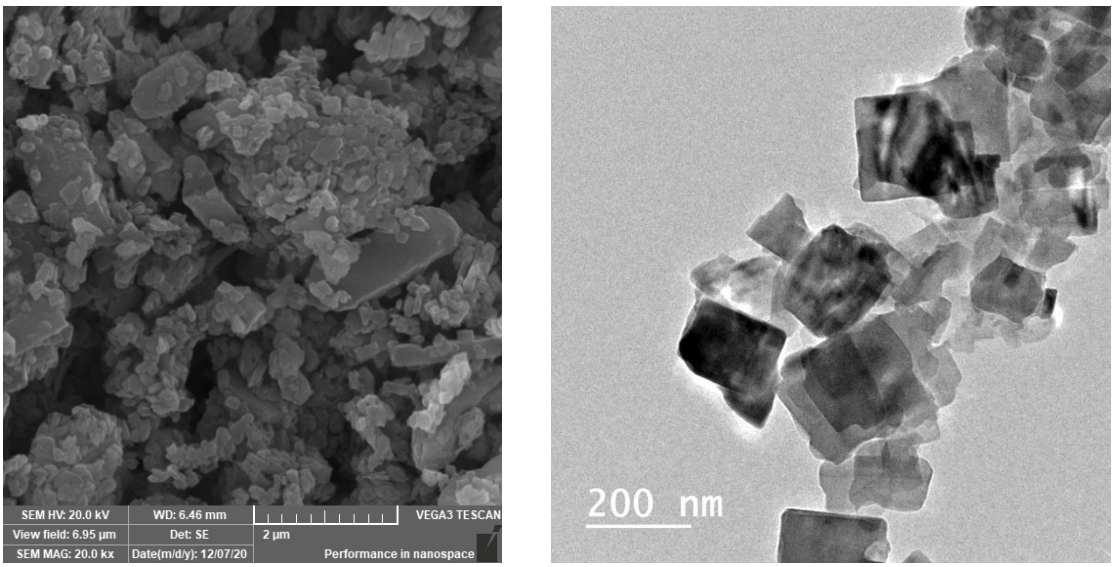

Fig. 4. (a) Scanning electron microscopy and (b) transmission electron microscopy of CuKHCF nanoparticles.

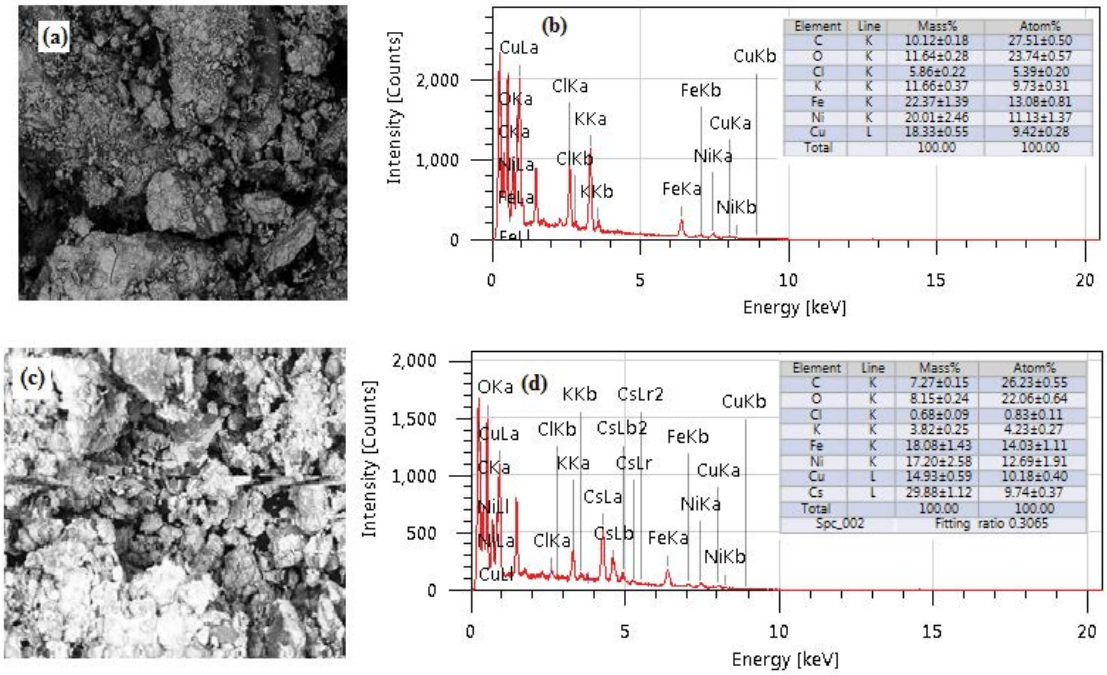

Fig. 5. Scanning electron microscopy-energy-dispersive X-ray spectroscopy for CuKHCF/O-CMC nanocomposite before and after cesium adsorption.

which having the same peaks that appear in Fig. 6a and b for CuKHCF and O-CMC. So, the XRD confirms the introducing of CuKHCF into the prepared O-CMC.

3.2.4. Thermal studies

The degradation stages of O-CMC and nanocomposite were investigated as through TGA (Fig. 7). For O-CMC (Fig. 7a), three decomposition stages were observed. The first one is related to the loss of water and started at 41.95°C to 176.67°C. The second stage starts at 179.45°C–325.10°C and the third step at 325.01°C–965.90°C. Second and the third stages related to decomposition of polysaccharide main chain through breaking glycosidic bonds (C–O–C) in addition to volatile product undergoes evaporation and elimination [36]. Fig. 7b shows that the decomposition steps of

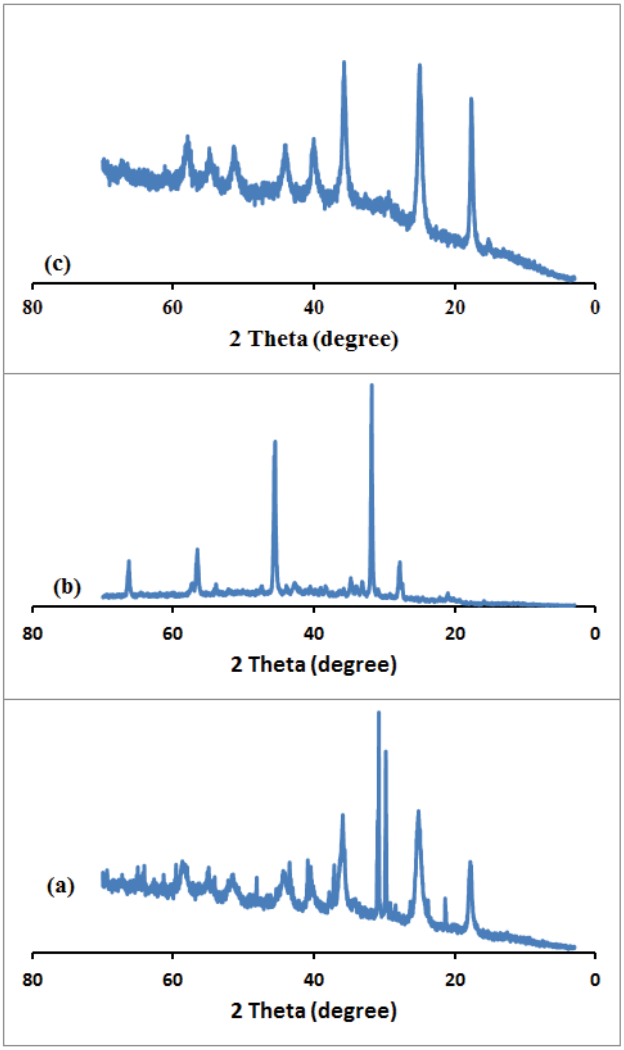

Fig. 6. X-ray diffraction for (a) CuKHCF nanoparticles, (b) O-CMC and (c) CuKHCF/O-CMC nanocomposite.

CuKHCF/O-CMC nanocomposite were achieved at temperatures higher than O-CMC. Which first stage was achieved in range of 42.16°C–203.85°C, while the second stage shifted to 201.82°C–413°C and the third step at 413.46–966.84. This shifting in temperatures confirmed the introducing of CuKHCF in O-CMC matrix that showed change in thermal properties in addition to increase the stability of prepared nanocomposite.

Also, differential thermogravimetric analysis (DTG) curves for O-CMC and nanocomposite were studied. For O-CMC (Fig. 7a), three peaks were observed. The first peak at 173°C, which is assigned to water loss found in crystal lattice. The second and third peaks are due to decomposition of polysaccharide main chain through breaking glycosidic bonds (C–O–C) in addition to volatile product undergoes evaporation and elimination, which occurs at 321°C and 501°C, respectively. Also, in DTG for nanocomposite (Fig. 7b), three peaks are shown but these peaks are shifted to higher temperatures at 204°C for first peak, 414°C for second peak and 649°C for third peak than appeared in DTG for O-CMC.

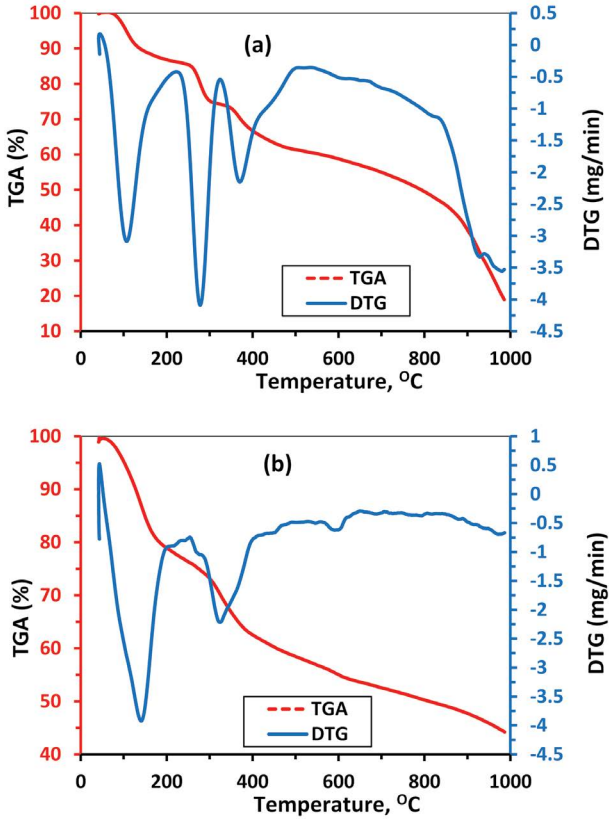

Fig. 7. Thermogravimetric analysis for (a) O-CMC and (b) CuKHCF/O-CMC nanocomposite.

3.3. Uptake of cesium ion using batch technique

3.3.1. Effect of pH of Cs solution

pH of Cs solutions has a great effect in the nature of sorption process, so it is necessary to study this factor. The experiments were carried out through fixed the amount of nanocomposite (0.1 g), volume of cesium solution (100 mL) of constant concentration (3 mmol/L) in addition to the shaking time (2 h) at 25°C. But solutions of different pH (2.5–11) were used. The results obtained from experiments showed that at the pH increase, the sorption capacity increased until the highest value at pH 7 and begin to decrease at basic media (Fig. 8). At low pH, low adsorption capacities obtained which this is may be due to the competition that occurred between Cs^+ and H^+ ions or the dissolution of CuKHCF/O-CMC nanocomposite in acidic media [32]. Also, results revealed that in basic media the capacity decreased. One of the following reasons can explain this observation: one of them is due to generation neutral Cs(OH) or $Cs(OH)_2^-$. Cesium in both forms has less affinity than positive form (Cs^+) [37]. Another reason is partially decomposition of CuKHCF from the surface of composite in basic medium [38,39].

3.3.2. Influence of the initial Cs concentration on sorption behavior of CuKHCF/O-CMC nanocomposite

Different concentrations of Cs^+ ions were treated with CuKHCF/O-CMC nanocomposite to study the sorption

behavior of Cs onto nanocomposite. All experiments were investigated by fixing pH 7, shaking time 2 h and temperature 25°C but only initial concentration of cesium is changed (1–14 mmol/L). Fig. 9 shows that the capacity enhanced with increasing in initial concentration of Cs ions until it remains constant at initial concentration 12 mmol/L. The optimum concentration of Cs ions was 10 mmol/L, which it recorded adsorption capacity 1.71 mmol/g.

3.3.2.1. Adsorption isotherm

The mechanism of sorption of Cs ions onto nanocomposite can be reported through three isotherm models. First model is Langmuir, which can be expressed by Eq. (9) [40]:

$$\frac{C_e}{q_e} = \frac{C_e}{Q_{\max}} + \frac{1}{KQ_{\max}} \tag{9}$$

where C_e (mmol/L) is the equilibrium concentration of Cs and q_e (mmol/g) is the calculated capacity obtained from Eq. (1). $Q_{\max}$ (mmol/g) is the obtained maximum capacity from slope and K (mmol^{-1}) is constant of Langmuir. The parameters obtained from Eq. (9) are collected in Table 1. R_L is one of essential characteristic for Langmuir model that obtained from the Eq. (10):

$$R_L = \frac{1}{1 + KC_0} \tag{10}$$

where K is Langmuir constant and C_0 is initial Cs concentration (mmol/L). The isotherm shape can be explained according to values of R_L. If the value of R_L is more than one, the sorption process is unfavorable. If R_L value equal to zero or one, this process is irreversible [32]. But this process becomes favorable in case of values of R_L lie between zero and one. Another important isotherm model namely Freundlich which assume that the process of sorption is heterogeneous. Eq. (11) can be used to express the Freundlich model [41]:

$$\log q = N \log C_e + \log K_F \tag{11}$$

where K_F (mmol/g) and N were pointed to Freundlich constants. Temkin model can be represented by Eq. (12) [42]:

$$q = B \ln K_T + B \ln C_e \tag{12}$$

where K_T (L/g) and B (J/mol) are constants of equilibrium binding and adsorption heat, respectively. From data obtained from Fig. 10 and collected in Table 1 for all isotherms models, Langmuir with correlation coefficient R^2 = 0.989 was preferred as model that can describe the sorption behaviors of CuKHCF/O-CMC than other isotherm models.

3.3.3. Effect of contact time between CuKHCF/O-CMC nanocomposite with Cs$^+$ solution and equilibrium kinetic models

The capacity of Cs$^+$ ions onto CuKHCF/O-CMC nanocomposite can be studied as a function of contact time (15–180 min). The conditions of experiments were optimized at pH = 7, Cs$^+$ concentration = 10 mmol/L, and 25°C. Fig. 11 showed that Cs$^+$ capacity onto CuKHCF/O-CMC nanocomposite was enhanced with increasing in contact time until achieving an equilibrium state.

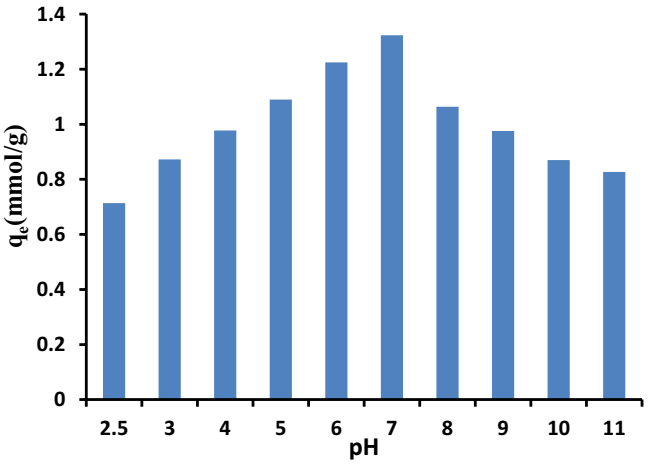

Fig. 8. Influence of pH of cesium solution on sorption behavior of CuKHCF/O-CMC nanocomposite.

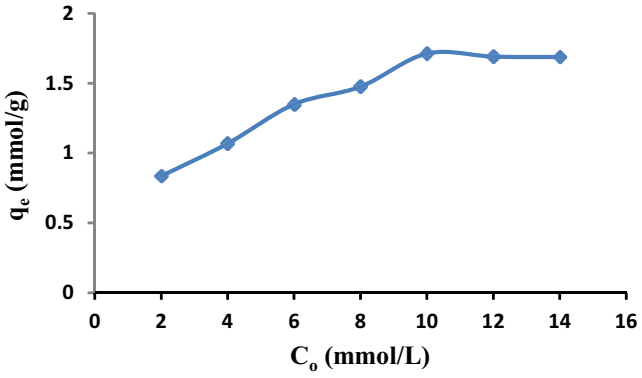

Fig. 9. Sorption behavior of different initial concentration of Cs onto CuKHCF/O-CMC nanocomposite.

Table 1
Isotherms data for Langmuir, Freundlich, and Temkin models

Metal ion	Langmuir				Freundlich			Temkin		
Cs	$Q_{\max}$	K	R^2	R_L	N	K_F	R^2	K_T	B	R^2
	2.006	0.485	0.989	0.129–0.508	0.327	0.793	0.968	6.068	0.406	0.955

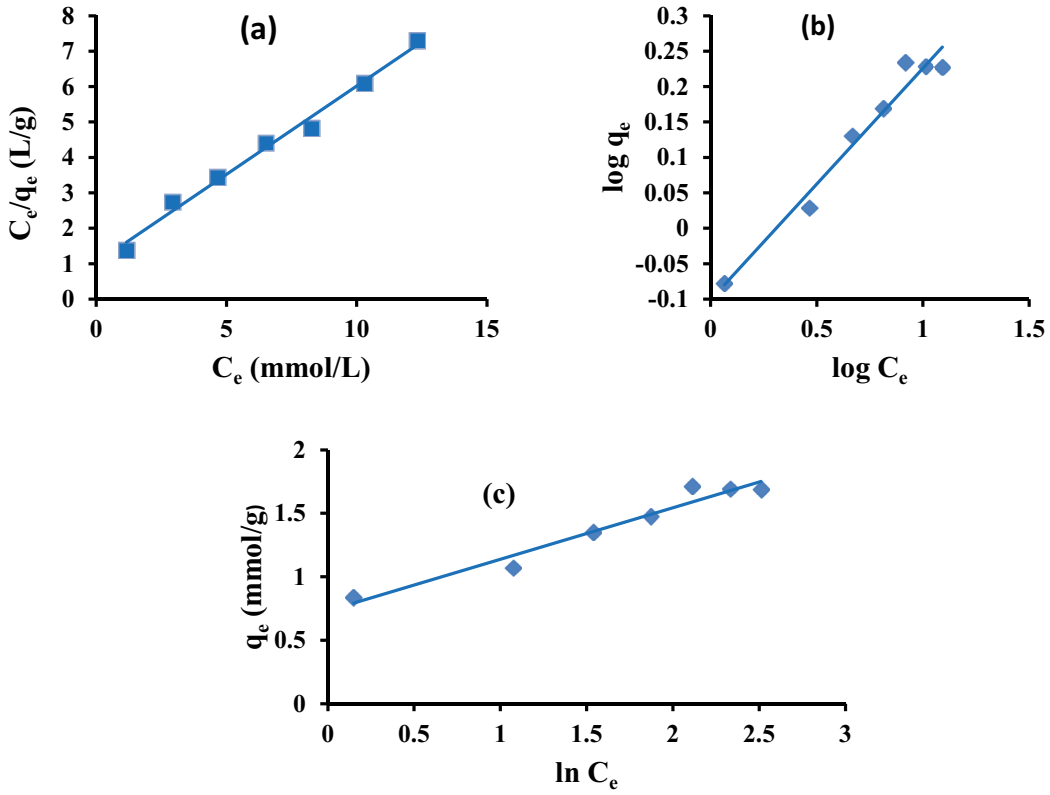

Fig. 10. Models of isotherms (a) Langmuir, (b) Freundlich and (c) Temkin.

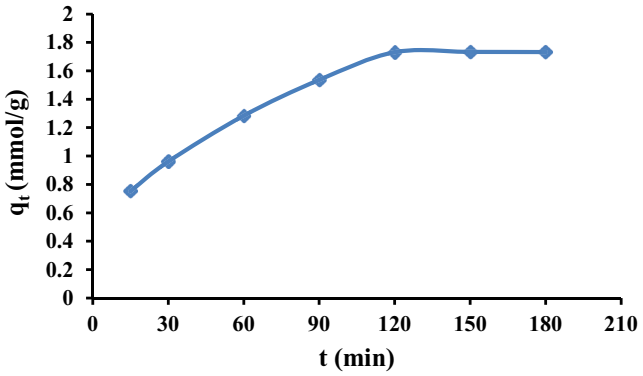

Fig. 11. Influence of contact time between CuKHCF/O-CMC nanocomposite with Cs solution on sorption process.

The kinetic of sorption process of Cs^+ can be investigated by three models, namely pseudo-first-order [Eq. (13)] [43], pseudo-second-order [Eq. (14)] [44] and intraparticle diffusion model [Eq. (15)] [45].

$$\log\left(q-q_t\right)=\log q-\left(\frac{K_{ads}}{2.303}\right)t \tag{13}$$

$$\frac{t}{q_t}=\frac{1}{K_2q^2}+\left(\frac{1}{q}\right)t \tag{14}$$

$$q_t=K_{id}t^{0.5} \tag{15}$$

where q and q_t are the capacities of Cs^+ (mmol/g) at equilibrium state and at any contact time (min), respectively. K_{ads} (min^{-1}) is first-order rate constant, K_2 (g/mmol·min) is second-order rate constant and k_{id} (mmol/g·$min^{0.5}$) is intraparticle diffusion models rate constant. In this work, three models (Fig.12) were applied to obtain some important parameters for explaining mechanism of sorption process. From data found in Table 2, pseudo-second-order kinetic model is fitted with sorption of Cs onto CuKHCF/O-CMC nanocomposite.

3.3.4. Thermodynamic studies

Sorption efficiency of Cs^+ onto nanocomposite was examined at different temperatures (25°C–55°C). Fig. 13 shows that the capacity of sorption of Cs^+ is increased with enhancing in solution temperature, which realized that, the endothermic nature of the process. Also, the natural of process can be explained through three thermodynamic parameters namely Gibbs free energy ($\Delta G°$) (kJ/mol), enthalpy change ($\Delta H°$) (kJ/mol) and entropy change ($\Delta S°$) (kJ/mol), that parameters can be estimated by using Eqs. (16) and (17):

$$\Delta G^\circ_{ads}=-RT\ln K_d \tag{16}$$

$$\ln K_d=\frac{\Delta S^\circ_{ads}}{R}-\frac{\Delta H^\circ_{ads}}{RT} \tag{17}$$

where T (K) and R (8.314 J/mol·K) are absolute temperature and universal gas constant, respectively. K_d (mL/g) is equilibrium distribution constant. K_d can be calculated by Eq. (18).

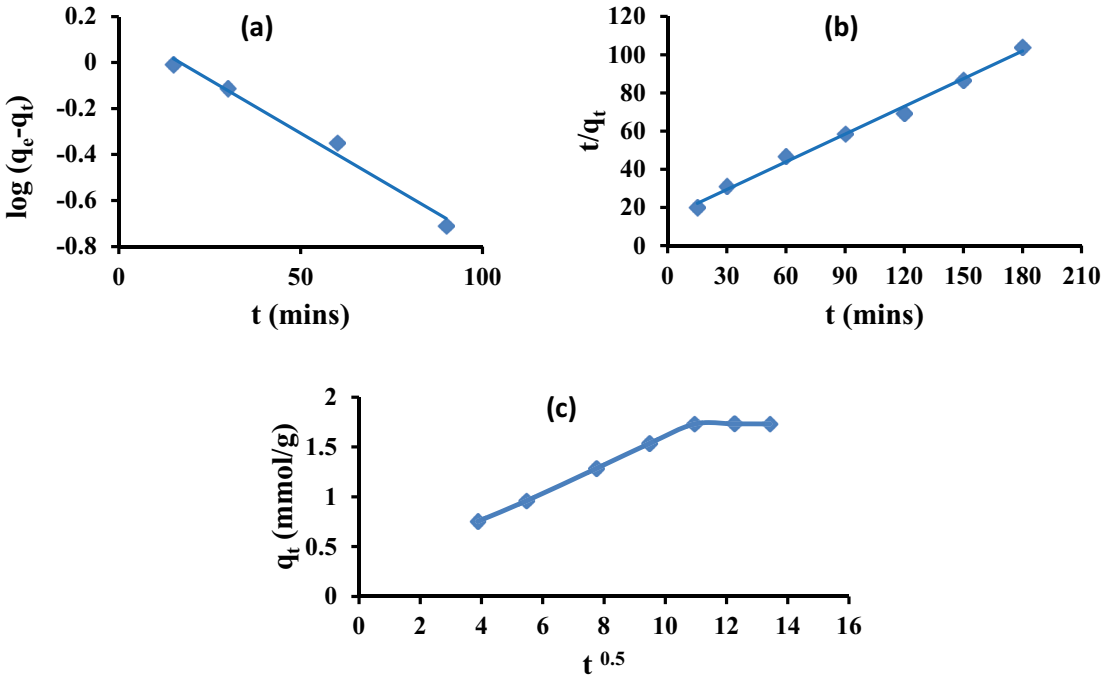

Fig. 12. Models of (a) pseudo-first-order, (b) pseudo-second-order and (c) intraparticle diffusion.

Table 2
Parameters for pseudo-first-order, pseudo-second-order and intraparticle diffusion

Metal ion	Pseudo-first-order			Pseudo-second-order			Intraparticle diffusion	
	q (mmol/g)	K_{ads} (1/min)	R^2	Q	K_2	R^2	k_{id}	R^2
Cs	1.433	0.021	0.985	2.0695	0.016	0.994	0.149	0.822

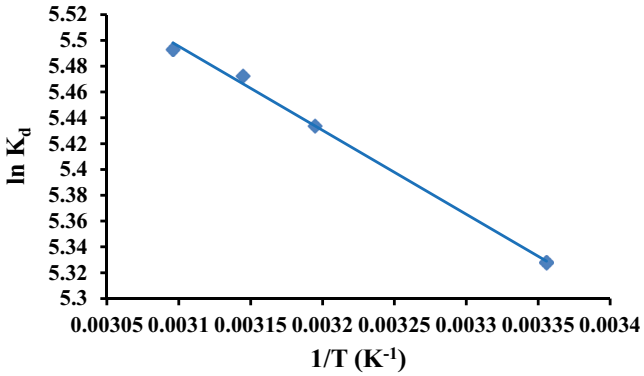

Fig. 13. Distribution coefficient for the Cs^+ ions sorption onto nanocomposite at different temperatures.

$$K_d = \frac{(C_0 - C_e)}{C_e} \times \frac{V}{W} \tag{18}$$

$\Delta H°$, $\Delta S°$ and $\Delta G°_{ads}$ are collected in Table 3. From these parameters, we concluded that the process is endothermic due to $\Delta H° = 5.4078$ kJ/mol > 0. That is meaning that the increasing in the solution temperature support the sorption process of Cs^+. The spontaneity and randomness of this process is realized due to negative values $\Delta G°_{ads}$ and positive value of $\Delta S°_{ads}$, respectively.

3.4. Fixed-bed column sorption

The dynamics of sorption column operation can be determined in large part by the timing and nature of the

Table 3
Obtained parameters for thermodynamic studies of sorption Cs^+ ions through the synthesized nanocomposite

Metal ion	$-\Delta G°_{ads}$ (kJ/mol)				$\Delta H°_{ads}$ (kJ/mol)	$\Delta S°_{ads}$ (kJ/mol)	R^2
	298 K	313 K	318 K	323 K			
Cs	13.200	14.140	14.468	14.751	5.4078	0.0625	0.9962

breakthrough. The breakthrough curves were created by graphing C_{eff}/C_0 vs. V_{eff} for Cs(I) sorption onto composite at different bed depths (0.8, 1.6, and 2.4 cm). At a fixed bed height of 1.6 cm, the impact of 1 and 3 mL/min flow rates was investigated. A fixed concentration of Cs^+ solution was prepared (C_o = 4 mmol/L) where the pH was optimally adjusted to be of 7. In Figs. 12 and 13 the breakthrough curves are displayed. Eqs. (2)–(8) were employed to calculate the composite sorption capacity (q_e) and removal percentage (R %) from the breakthrough curves. The findings are displayed in Table 4.

3.4.1. Influence of bed height

Cs^+ adsorption was investigated on a continuous flow rates of 1 mL/min in a fixed bed column, 4 mmol/L Cs^+ concentration, pH = 7, and different bed heights (0.8, 1.6, and 2.4 cm). Table 4 provides the breakthrough analyses, and Fig. 14 displays the breakthrough curves for Cs^+ sorption at various heights of the beds. After the breakthrough point in various curves, the adsorption of Cs^+ persisted, and there would be a sharp rise in C_{eff}/C_o then steadily moves creating an S-shaped curve. As indicated in Table 4, the breakthrough time (t_b) and exhaust time (t_e), increased when the height of the bed rose. Hence, a rise in the Cs^+ removal percentage (R %) was noted. This rise in removal % could be caused by the rise in binding sites on the composite existing for adsorption. Also, it takes longer for the transfer zone to get to the end of the column so that Cs^+ might have more time to come into touch with the composite. In light of this, a bigger mass transfer zone will arise from raising the height of the bed as seen in Fig. 14, as the breakthrough curves will be rather gradual. In contrast, at a fixed flow rate as the bed length extended, Z_m value increased. Tripled the length of the bed results in the overall removal percentage (R %) of Cs^+ went raised by 25% because a bigger volume of Cs^+ solution may receive treatment and a greater proportion will adsorb of Cs^+ at longer beds (Table 4). The maximal saturation of the all adsorbent's active sites dose by metal ions and the wide ending mass transfer region must be connected to the rise in percentage removal. Additionally, the bed capacities were enhanced from 0.96764 to 1.212 mmol/g by using a rise of 0.8 to 2.4 cm in the depth of the bed. These findings support earlier research findings [46,47].

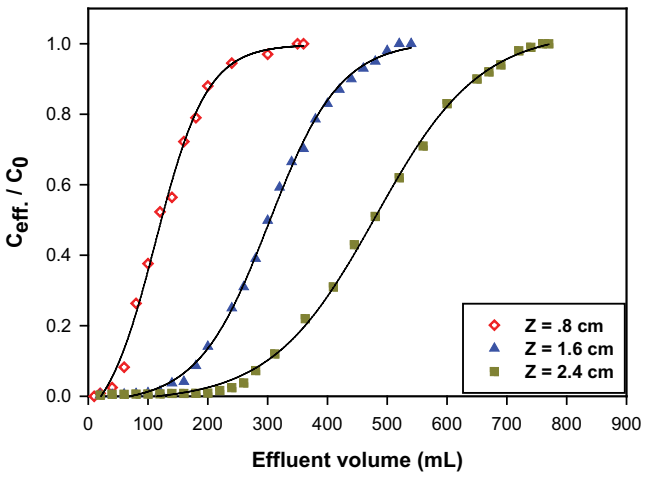

Fig. 14. Breakthrough curves for Cs^+ adsorption onto composite; flow rate is 1 mL/min, starting concentration is 4 mmol/L, the operating temperature is 25°C, pH is 7 and different bed heights (0.8, 1.6, and 2.4 cm).

3.4.2. Influence of flow rate

The composite's breakthrough curves for removing Cs^+ at various flow rates of (1,3 mL/min) via a Cs^+ concentration of 4 mmol/L, pH = 7, and a column with bed height of 1.6 cm are shown in Fig. 15. Table 4 lists the parameters for breakthrough curves. The findings proved that raising a flow rate ranging from 1 to 3 mL/min produced a decrease in both the time of exhaustion (t_e) and the time of breakthrough (t_b), with a changes in the breakthrough curves towards the low time span.

In general, when the flow rate was lower, the Cs^+ adsorption grew with longer times of contact. Raising the flow rate prevents all Cs^+ from having ample time to pass via the pores of the composite from the solution, resulting in a reduction in Cs^+ removal. Nevertheless, rising from 1 to 3 mL/min of flow rate results in a 7% (Table 4) reduction in the percentage removal of Cs^+ because Cs^+ exited the column before it reached equilibrium. Table 4 displays how when the flow rate raises, the capacity for adsorption at equilibrium (q_e) decreases. So, in this investigation, the 1 mL/min flow rate with the maximum capacity for adsorption (q_e) would be utilized. In addition, with varied flow rates, Z_m length values are near, because may be related to the same cause that both the time of exhaustion (t_e) and the time of breakthrough (t_b) get shorter as flow rate rises [48].

Table 4
Parameters for column data, Yoon–Nelson and Thomas model constants at various bed heights and flow rates (C_o = 4 mmol/L)

Variables			Calculated parameters				Thomas model			Yoon–Nelson model			
Metal ion	F (mL/min)	Z (cm)	q_{total} (mmoL)	q_e (mmol/g)	R %	Z_m (cm)	q_e (mmol/g)	K_{Th} (L/mmol·min)	R^2	K_{YN} (min^{-1})	τ (min)	R^2	τ_{exp} (min)
	1	0.8	0.48382	0.96764	34.56	0.7543	1.033	0.00725	0.9232	0.029	128.855	0.9232	116.87
	1	1.6	1.14408	1.14408	55	1.2923	1.214	0.0049	0.9916	0.0196	313.857	0.9916	300.32
Cs(I)	1	2.4	1.81744	1.212	59.784	1.7684	1.265	0.003475	0.9814	0.0139	474.37	0.9814	475.625
	1	1.6	1.14408	1.14408	55	1.2923	1.214	0.0049	0.9916	0.0196	313.857	0.9916	300.32
	3	1.6	0.6115	0.6115	47.77	1.4	0.6309	0.024525	0.9949	0.0981	52.5790	0.9949	53.333

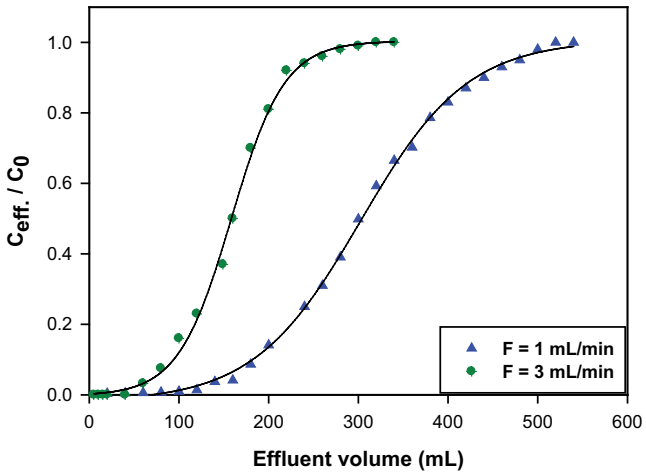

Fig. 15. Breakthrough curves for Cs^+ adsorption onto composite; starting concentration is 4 mmol/L, bed height is 1.6 cm, pH = 7 and at 25°C and different flow rates (1 and 3 mL/min).

3.4.3. Breakthrough curves models

The experimenting findings concerning the pattern of the solute interaction were shown, as well as the breakthrough curves were estimated, using a variety of models of theory, including the models created by Yoon–Nelson as well as Thomas [49–51].

3.4.3.1. Thomas model

As a way to find out the composite specific sorption capacity at equilibrium and kinetic constant at various influent flow rates as well as bed depths, this data was fitted to the modeled of Thomas [52]. In order for this model to work, it is assumed that (i) there is no axial dispersion in the fixed bed column and (ii) this sorption process is characterized by a pseudo-second-order reaction rate theory that lowers the Langmuir isotherm at equilibrium. Eq. (19) gives the Thomas model's linearized form:

$$\ln\left(\frac{C_0}{C_{\text{eff}}}-1\right)=\frac{K_{\text{Th}}q_eW}{F}-\frac{K_{\text{Th}}C_0}{F}V_{\text{eff}} \tag{19}$$

where q_e is the adsorption capacity of Cs^+ ion on the composite in millimoles per g, K_{Th} is the Thomas rate constant in litre per millimoles per minute, C_0 is the concentration of influent single metal ions in millimoles per litre, W is the column's composite dosage in grammes, C_{eff} is the effluent concentration at time t in millimoles per liter, and F is the flow rate in mL/min. To calculate the adsorbent's maximal capacity for adsorption and its kinetic coefficient in the Thomas model, Eq. (19) was fitted with experimental data. By graphing $\ln[(C_0/C_{\text{eff}}) - 1]$ vs. V_{eff}, the above equation was utilized to match the experimental acquired data. The slope and intercept were employed to determine the maximum ion exchange capacity as well as the Thomas rate constant, respectively. Table 4 provides these two parameters' values. Table 4 demonstrates that the experimental q_e and the Thomas model's q_e are comparable. In addition, Table 4 demonstrates that this Cs^+ Thomas rate constant decreased when the bed's height rose and rose when the flow rate was higher, although the value of q_e reduced with a higher flow rate and rose with a higher bed height. As may be seen, the experimental data and theoretical results correspond rather well.

3.4.3.2. Yoon–Nelson model

Model of Yoon–Nelson, as stated via Eq. (20), is built upon the notion that the likelihood of adsorbate breakthrough on the adsorbent is exactly proportional to the reduction in adsorption for each adsorbate molecule. The Yoon–Nelson model with linearization is given by the Eq. (20) [53]:

$$\ln\frac{C_{\text{eff}}}{C_0-C_{\text{eff}}}=\frac{K_{\text{YN}}}{F}V_{\text{eff}}-\tau K_{\text{YN}} \tag{20}$$

where the sampling time is t (min), the time needed for 50% exchange breakthrough is τ (min), and the Yoon–Nelson rate constant is K_{YN} (min^{-1}). In order to calculate a rate constant (K_{YN}) and the length of time necessary to achieve 50% adsorbate breakthrough (τ) in the model of Yoon–Nelson, Data from experiments were fitted into Eq. (20). In order to fit the experimentally collected data, this equation was employed by graphing $\ln(C_{\text{eff}}/(C_0 - C_{\text{eff}}))$ against the effluent volume (V_{eff}). From the slope and intercept, the Yoon–Nelson rate constant (K_{YN}) as well as the amount of time needed to achieve 50% adsorbate breakthrough (τ) were calculated, respectively. In Table 4, two parameters' values are displayed. Data contained in Table 4 further demonstrates that τ_{cal} and τ_{exp} are close to one another; this implies that the experimental results from the fixed bed column fitted well with the Yoon–Nelson model. It was shown that increasing flow rate caused the rate constant K_{YN} for Cs^+ from a single solution to rise, but increasing bed depth caused it to drop. As a result of metal ions spending less time in the adsorbent bed, it was also demonstrated that the time needed to achieve 50% adsorbate breakthrough for Cs^+ increased with bed height rather than decreasing as the flow rate increased. Given that the model and experimental results agree well. The models of Yoon–Nelson and Thomas were discovered to be useful for capturing all or a particular component of continuous operations' dynamic behavior. As shown in Eqs. (19) and (20), the linear equations for the models of Thomas and Yoon–Nelson may be given. According to the equations, each model has identical R^2 values as well as a projected breakthrough curve. The model of Thomas examines the impact of adsorption capacity, whereas the model of Yoon–Nelson forecasts the time needed to achieve a 50% breakthrough. These facts aid in demonstrating the effectiveness of every model separately.

3.5. Column regeneration

Examining the composite's ability for regeneration across a number of cycles is crucial from an economic perspective. In the current study, composite was used five times for repeated adsorption–desorption cycles at a bed height of 1.6 cm, a flow rate of 1 mL/min, and a Cs^+ concentration

of 4 mmol/L. The composite was utilized once more in subsequent sorption experiments following the elution of each column by 2.0 M KCl. The sorption–desorption cycle findings demonstrate that the composite's adsorption capacity was considerably influenced after five iterations of regeneration; after five cycles, the adsorption capacity fell from 100% to 88%. According to these findings, composite is a long-lasting adsorbent with a strong capacity to challenge industrial adsorbents in terms of cost viability.

4. Conclusion

An effective ion exchanger polymer nanocomposite was achieved and used for extraction of Cs ions in aqueous media. The ion exchanger polymer nanocomposite was prepared based on natural polymer with some chemical modification. The reaction followed by three steps to prepare the ion exchanger, the first step including formation of O-carboxymethyl chitosan (O-CMC), the second step is the formation copper potassium hexacyanoferrates nanoparticles (CuKHCF) and finally the prepared CuKHCF was incorporated through polymer matrix of O-CMC to obtain CuKHCF/O-CMC. By FTIR, the composition of the prepared compounds was elucidated, whereas the surface morphology of nanoparticles of CuKHCF and ion exchanger was reported by SEM and TEM. Also, the thermal behavior was studied using TGA and DTG. The sorption behavior of the prepared ion exchanger toward Cs ions in aqueous media was investigated through batch and column technique. The elucidated results showed that the highest capacity was 1.71 mmol/g for Cs ions with initial concentration 10 mmol/L and shaking time 2 h at temperature 25°C. The obtained data from isotherms and the kinetics showed that Langmuir and pseudo-second-order are fitted with this process. Also, thermodynamics parameters showed the endothermic and spontaneous natural of the sorption process. The sorption process was also achieved by column technique. Also, models of Thomas and Yoon–Nelson were employed to assess the performance of the column adsorption. Examining the composite's ability for regeneration was studied through five times for repeated adsorption–desorption cycles at a bed height of 1.6 cm, a flow rate of 1 mL/min, and a Cs^+ concentration of 4 mmol/L. The composite was utilized once more in subsequent sorption experiments following the elution of each column by 2.0 M KCl.

Institutional review board statement

The study was conducted and approved according to the guidelines of the declaration of the ethical committee of the Faculty of Science, Benha University (No. 43 chm).

References

[1] J.T. Smith, S.M. Wright, M.A. Cross, L. Monte, A.V. Kudelsky, R. Saxén, S.M. Vakulovsky, D.N. Timms, Global analysis of the riverine transport of ^{90}Sr and ^{137}Cs, Environ. Sci. Technol., 38 (2004) 850–857.

[2] J.L. Mertz, Z.H. Fard, C.D. Malliakas, M.J. Manos, M.G. Kanatzidis, Selective removal of Cs^+, Sr^{2+}, and Ni^{2+} by $K_{2x}Mg_xSn_{3-x}S_6$ (x = 0.5–1) (KMS-2) relevant to nuclear waste remediation, Chem. Mater., 25 (2013) 2116–2127.

[3] Y. Namiki, T. Namiki, Y. Ishii, S. Koido, Y. Nagase, A. Tsubota, N. Tada, Y. Kitamoto, Inorganic-organic magnetic nanocomposites for use in preventive medicine: a rapid and reliable elimination system for cesium, Pharm. Res., 29 (2012) 1404–1418.

[4] H. Yoshikawa, S. Sunada, H. Hirakawa, A. Fujimori, S. Elmegerhi, D. Leary, T. Kato, Radiobiological characterization of canine malignant melanoma cell lines with different types of ionizing radiation and efficacy evaluation with cytotoxic agents, Int. J. Mol. Sci., 20 (2019) 841, doi: 10.3390/ijms20040841.

[5] O. Artun, Study of nuclear structure for ^{244}Cm, ^{241}Am, ^{238}Pu, ^{210}Po, ^{147}Pm, ^{137}Cs, ^{90}Sr and ^{63}Ni nuclei used in nuclear battery, Mod. Phys. Lett. A, 32 (2017) 1750117, doi: 10.1142/S0217732317501176.

[6] C.T.K. Chusreeaeom, M.L.N. Sukin, P. Jompuk, Comparative effect of high energy electron beam and ^{137}Cs gamma ray on survival, growth and chlorophyll content in curcuma hybrid 'Laddawan' and determine proper dose for mutations breeding, Emirates J. Food Agric., 31 (2019) 321–327.

[7] K. Shakir, M.Sohsah, M. Soliman, Removal of cesium from aqueous solutions and radioactive waste simulants by coprecipitate flotation, Sep. Purif. Technol., 54 (2007) 373–381.

[8] C. Xu, J.C. Wang, J. Chen, Solvent extraction of strontium and cesium: a review of recent progress, Solvent Extr. Ion Exch., 30 (2012) 623–650.

[9] F. Jia, J.F. Li, J.L. Wang, Y.L. Sun, Removal of cesium from simulated radioactive wastewater using a novel disc tubular reverse osmosis system, Nucl. Technol., 197 (2017) 219–224.

[10] J.L. Wang, S.T. Zhuang, Removal of cesium ions from aqueous solutions using various separation technologies, Rev. Environ. Sci. Biotechnol., 18 (2019) 231–269.

[11] M. Adabbo, D. Caputo, B. de Gennaro, M. Pansini, C. Colella, Ion exchange selectivity of phillipsite for Cs and Sr as a function of framework composition, Microporous Mesoporous Mater., 28 (1999) 315–324.

[12] L. Lalhmunsiama, C. Lalhriatpuia, D. Tiwari, S.-M. Lee, Immobilized nickel hexacyanoferrate on activated carbons for efficient attenuation of radio toxic Cs(I) from aqueous solutions, Appl. Surf. Sci., 321 (2014) 275–282.

[13] T. Vincent, C. Vincent, Y. Barré, Y. Guari, G. Le Saout, E. Guibal, Immobilization of metal hexacyanoferrates in chitin beads for cesium sorption: synthesis and characterization, J. Mater. Chem. A, 2 (2014) 10007–10021.

[14] T. Vincent, C. Vincent, E. Guibal, Immobilization of metal hexacyanoferrates ion exchangers for the synthesis of metal ion sorbents, Molecules, 20 (2015) 20582–20613.

[15] Y. Kim, Y.K. Kim, S. Kim, D. Harbottle, J.W. Lee, Nanostructrued potassium copper hexacyanoferrate-cellulose hydrogel for selective and rapid cesium adsorption, Chem. Eng. J., 313 (2017) 1042–1050.

[16] Y. Zong, Y. Zhang, X. Lin, D. Ye, D. Qiao, S. Zeng, Facile synthesis of potassium copper ferrocyanide composite particles for selective cesium removal from wastewater in the batch and continuous processes, RSC Adv., 7 (2017) 31352–31364.

[17] Y.K. Kim, T. Kim, Y. Kim, D. Harbottle, J.W. Lee, Highly effective Cs^+ removal by turbidity-free potassium copper hexacyanoferrate-immobilized magnetic hydrogels, J. Hazard. Mater., 340 (2017) 130–139.

[18] Y.K. Kim, Y. Kim, S. Kim, D. Harbottle, J.W. Lee, Solvent-assisted synthesis of potassium copper hexacyanoferrate embedded 3D-interconnected porous hydrogel for highly selective and rapid cesium ion removal, J. Environ. Chem. Eng., 5 (2017) 975–986.

[19] Y.K. Kim, K. Bae, Y. Kim, D. Harbottle, J.W. Lee, Immobilization of potassium copper hexacyanoferrate in doubly crosslinked magnetic polymer bead for highly effective Cs^+ removal and facile recovery, J. Ind. Eng. Chem., 68 (2018) 48–56.

[20] J.Y. Yoon, H. Zhang, Y.K. Kim, D. Harbottle, J.W. Lee, A high-strength polyvinyl alcohol hydrogel membrane crosslinked by sulfosuccinic acid for strontium removal via filtration, J. Environ. Chem. Eng., 7 (2019) 102824, doi: 10.1016/j.jece.2018.102824.

[21] K.-M. Lee, T. Kawamoto, K. Minami, A. Takahashi, D. Parajuli, G. Kido, K. Yoshino, H. Tanaka, Improved adsorption properties of granulated copper hexacyanoferrate with multi-scale porous networks, RSC Adv., 6 (2016) 16234–16238.
[22] B. Folch, J. Larionova, Y. Guari, K. Molvinger, C. Luna, C. Sangregorio, C. Innocenti, A. Caneschi, C. Guerin, Synthesis and studies of water-soluble Prussian blue type nanoparticles into chitosan beads, Phys. Chem. Chem. Phys., 12 (2010) 12760–12770.
[23] D. Dechojarassri, S. Asaina, S. Omote, K. Nishida, T. Furuike, H. Tamura, Adsorption and desorption behaviors of cesium on rayon fibers coated with chitosan immobilized with Prussian blue, Int. J. Biol. Macromol., 104 (2017) 1509–1516.
[24] R. Wang, S. Gao, Z. Yang, Y. Li, W. Chen, B. Wu, W. Wu, Engineered and laser-processed chitosan biopolymers for sustainable and biodegradable triboelectric power generation, Adv. Mater., 30 (2018) 1706267, doi: 10.1002/adma.201706267.
[25] E. Szymanska, K. Winnicka, Stability of chitosan – a challenge for pharmaceutical and biomedical applications, Mar. Drugs, 13 (2015) 1819–1846.
[26] S. Yang, D. Shao, X. Wang, G. Hou, M. Nagatsu, X. Tan, X. Ren, J. Yu, Design of chitosan–grafted carbon nanotubes: evaluation of how the –OH functional group affects Cs^+ adsorption, Mar. Drugs, 13 (2015) 3116–3131.
[27] P.S. Barber, S.P. Kelley, C.S. Griggs, S. Wallace, R.D. Rogers, Surface modification of ionic liquid-spun chitin fibers for the extraction of uranium from sea water: seeking the strength of chitin and the chemical functionality of chitosan, Green Chem., 16 (2014) 1828–1836.
[28] S. Chatterjee, M.W. Lee, S.H. Woo, Adsorption of Congo red by chitosan hydrogel beads impregnated with carbon nanotubes, Bioresour. Technol., 101 (2010) 1800–1806.
[29] J. Duan, X. Liang, Y. Cao, S. Wang, L. Zhang, High strength chitosan hydrogels with biocompatibility via new avenue based on constructing nanofibrous architecture, Macromolecules, 48 (2015) 2706–2714.
[30] L. Lv, N. Chen, C. Feng, Y. Gao, M. Li, Xanhate-modified magnetic chitosan/poly(vinyl alcohol) adsorbent: preparation, characterization, and performance of Pb(II) removal from aqueous solution, J. Taiwan Inst. Chem. Eng., 78 (2017) 485–492.
[31] M.K. Sureshkumar, D. Das, M.B. Mallia, P.C. Gupta, Adsorption of uranium from aqueous solution using chitosan-tripolyhosphate (CTPP) beads, J. Hazard. Mater., 184 (2010) 65–72.
[32] A.M. Metwally, M.M. Azab, A.A. Mahmoud, H.M. Ali, A.F. Shaaban, Core–shell polymer nanocomposite based on free radical copolymerization of anthranilic acid and o-amino phenol in the presence of copper hexacyanoferrates nanoparticles and its adsorption properties, J. Polym. Res., 29 (2022) 98, doi: 10.1007/s10965-022-02933-7.
[33] B. Preetha, T. Viruthagiri, Batch and continuous biosorption of chromium(VI) by *Rhizopus arrhizus*, Sep. Purif. Technol., 57 (2007) 126–133.
[34] S.H. Hasan, B.N. Bhattacharjee, P. Srivastava, Batch and continuous biosorption of Cu^{2+} by immobilised biomass of *Arthrobacter* sp., J. Environ. Manage., 90 (2009) 3313–3321.
[35] H. Ammar, A.F. Shabaan, S.M. El-Bahy, H.A. Elkhawaga, A.M. Metwally, Removal of uranium ions from aqueous solutions using nano-sized copper potassium hexacyanoferrate encapsulated O-carboxymethyl chitosan matrix by batch and fixed bed column methods, Desal. Water Treat., 291 (2023) 117–130.
[36] H. Zhang, H. Zhong, L. Zhang, S. Chen, Y. Zhao, Y. Zhu, Synthesis and characterization of thermosensitive graft copolymer of *N*-isopropylacrylamide with biodegradable carboxymethylchitosan, Carbohydr. Polym., 77 (2009) 785–790.
[37] P.A. Haas, A review of information on ferrocyanide solids for removal of cesium from solutions, Sep. Sci. Technol., 28 (1993) 2479–2506.
[38] Y. Kim, H.H. Eom, D. Kim, D. Harbottle, J.W. Lee, Adsorptive removal of cesium by electrospun nanofibers embedded with potassium copper hexacyanoferrate, Sep. Sci. Technol., 255 (2021) 117745, doi: 10.1016/j.seppur.2020.117745.
[39] S.M. El-Bahy, D.A. Fadel, Z.M. El-Bahy, A.M. Metwally, Rapid and highly efficient cesium removal by newly synthesized carbomer encapsulated potassium copper hexacyanoferrate composite, J. Environ. Chem. Eng., 6 (2018) 1875–1885.
[40] I. Langmuir, The adsorption of gases on plane surfaces of glass, mica and platinum, J. Am. Chem. Soc., 40 (1918) 1361–1403.
[41] H. Freundlich, Adsorption in solution, Phys. Chem. Soc., 40 (1906) 1361–1368.
[42] M.J. Temkin, V. Phyzev, Recent modifications to Langmuir isotherms, Acta Physiochim. USSR, 12 (1940) 217–222.
[43] S. Lagergren, Zur theorie der sogenannten adsorption gelöster stoffe, Kungliga Svenska Vetenskapsakademiens, Handlingar, 24 (1898) 1–39.
[44] Y.S. Ho, Second-order kinetic model for the sorption of cadmium on to tree fern: a comparison of linear and nonlinear methods, Water Res., 40 (2006) 119–125.
[45] W.J. Weber, J.C. Morris, Equilibria and capacities for adsorption on carbon, J. Sanit. Eng. Div., 90 (1964) 79–91.
[46] T.S. Singh, K.K. Pant, Experimental and modelling studies on fixed bed adsorption of As(III) ions from aqueous solution, Sep. Purif. Technol., 48 (2006) 288–296.
[47] Z. Yu, T. Qi, J. Qu, Y. Guo, Application of mathematical models for ion-exchange removal of calcium ions from potassium chromate solutions by Amberlite IRC 748 resin in a continuous fixed bed column, Hydrometallurgy, 158 (2015) 165–171.
[48] H. Muhamad, H. Doan, A. Lohi, Batch and continuous fixed-bed column biosorption of Cd^{2+} and Cu^{2+}, Chem. Eng. J., 158 (2010) 369–377.
[49] R. Han, D. Ding, Y. Xu, W. Zou, Y. Wang, Y. Li, L. Zou, Use of rice husk for the adsorption of Congo red from aqueous solution in column mode, Bioresour. Technol., 99 (2008) 2938–2946.
[50] R. Han, Yu. Wang, X. Zhao, Y. Wang, F. Xie, J. Cheng, M. Tang, Adsorption of methylene blue by phoenix tree leaf powder in a fixed-bed column: experiments and prediction of breakthrough curves, Desalination, 245 (2009) 284–297.
[51] M. Calero, F. Hernáinz, G. Blázquez, G. Tenorio, M.A. MartínLara, Study of Cr(III) biosorption in a fixed-bed column, J. Hazard. Mater., 171 (2009) 886–893.
[52] H.C. Thomas, Heterogeneous ion exchange in a flowing system, J. Am. Chem. Soc., 66 (1944) 1664–1666.
[53] Y.H. Yoon, J.H. Nelson, Application of gas adsorption kinetics 1. A theoretical model for respirator cartridge service time, Am. Ind. Hyg. Assoc. J., 45 (1984) 509–516.